Gamma-ray Time Delay and Magnification Ratio in the Gravitationally-Lensed Blazar PKS 1830-211

S. Buson , ^{1,2} M. De Toma, ³ S. Larsson, ^{4,5} C. C. Cheung, ⁶ P. Cristarella Orestano, ^{7,8} S. Ciprini, ^{9,10} C. Spingola, ¹¹ M. Razzano, ^{12,13} A. Dominguez, ¹⁴ M. Ajello, ¹⁵ and S. Cutini⁷

 Julius-Maximilians-Universität Würzburg, Fakultät für Physik und Astronomie, Institut für Theoretische Physik und Astrophysik, Lehrstuhl für Astronomie, Emil-Fischer-Str. 31, D-97074 Würzburg, Germany
 Deutsches Elektronen-Synchrotron DESY, Platanenallee 6, 15738 Zeuthen, Germany
 SISSA, via Bonomea 265, I-34135 Trieste, Italy

⁴Department of Physics, KTH Royal Institute of Technology, AlbaNova, SE-106 91 Stockholm, Sweden

⁵The Oskar Klein Centre for Cosmoparticle Physics, AlbaNova, SE-106 91 Stockholm, Sweden

⁶Space Science Division, Naval Research Laboratory, Washington, DC 20375, USA

⁷Istituto Nazionale di Fisica Nucleare, Sezione di Perugia, I-06123 Perugia, Italy

⁸Dipartimento di Fisica, Università degli Studi di Perugia, I-06123 Perugia, Italy

⁹Istituto Nazionale di Fisica Nucleare, Sezione di Roma "Tor Vergata," I-00133 Roma, Italy

¹⁰Space Science Data Center - Agenzia Spaziale Italiana, Via del Politecnico, snc, I-00133, Roma, Italy

¹¹INAF - Istituto di Radioastronomia, Via Gobetti 101, I-40129, Bologna, Italy

12 Department of Physics, University of Pisa, Largo B. Pontecorvo, 3, 56127, Pisa, Italy
 13 Istituto Nazionale di Fisica Nucleare, Sezione di Pisa, Largo B. Pontecorvo, 3, 56127, Pisa, Italy
 14 IPARCOS and Department of EMFTEL, Universidad Complutense de Madrid, E-28040 Madrid, Spain
 15 Department of Physics and Astronomy, Clemson University, Kinard Lab of Physics, Clemson, SC 29634-0978, USA

(Received November 25, 2025; Revised November 25, 2025)

ABSTRACT

We present the characterization of macrolensing properties of the gravitationally lensed system PKS 1830-211, utilizing data from the Fermi Large Area Telescope. While at γ -rays we can not spatially resolve the lensed images, a macrolensing-induced time pattern is expected in the blazar's lightcurve, resulting from the delay between variable γ -ray components originating from its two brightest lensed images. Compared to our previous study, here we employ high-quality lightcurves coupled with prolonged outburst activity, and improved time-series techniques. Analyzing six independent data segments, we identified a delay of 20.26 ± 0.62 days (statistical and stochastic uncertainty), with a chance detection probability at the 2.5×10^{-5} level (post-trial). We also present a novel approach to the magnification ratio estimate based on a comparison with simulated data. Our work suggests that the γ -ray flux ratio between the two main lens components is $\mu_{\gamma} \lesssim 1.8$. We do not observe convincing evidence of microlensing effects, as previously claimed. The measured γ -ray time delay is in 2σ tension with radio-based estimates, suggesting either distinct emission sites, underestimated radio uncertainties, or γ -ray production in a region opaque to radio. Our study highlights the potential of well sampled lightcurves and advanced time-series techniques to distinguish true lensing-induced delays from stochastic variability. When combined with improved radio constraints and refined lens models, PKS 1830–211 and similar sources constitute promising systems for time-delay cosmography, offering new insights into both jet structure and cosmological parameters.

Keywords: Galaxies: active — gravitational lensing: strong — gamma rays: galaxies — quasars: individual (PKS 1830-211)

1. INTRODUCTION

Email: sara.buson@desy.de, mdetoma@sissa.it, stefan@astro.su.se

Gravitational lensing presents a distinctive opportunity for probing mass distributions across the Universe and measuring the Hubble constant (H_0) . Recent stud-

ies have demonstrated the efficacy of this approach in cosmological investigations using the time-delay cosmography method (S. Refsdal 1964; see also findings from the H0LiCOW collaboration V. Bonvin et al. 2017). At the same time, they highlighted the importance of accurate time-delay measurements in lensed systems.

The system PKS 1830-211 is a notable example of strong gravitational lensing. Initially catalogued as a bright radio source at 5 GHz in the Parkes survey (C. Lidman et al. 1999), later observations by the Very Large Array (VLA) and Australian Telescope Compact Array (ATCA) revealed a lensed system composed of two compact highly magnified components (hereafter images A and B, to the northeast and southwest, respectively) separated by $\sim 1''$ and surrounded by an Einstein ring (A. Pramesh Rao & R. Subrahmanyan 1988; D. L. Jauncey et al. 1991). The lensed background object is a flat-spectrum-radio-quasar (FSRQ) at redshift z=2.507. Evidence for an additional fainter component has been tentatively discussed (R. Subrahmanyan et al. 1990; S. Nair et al. 1993) with the most recent ALMA observations pinpointing a point-like radio source, $\sim 0.3''$ away from image B, attributed as the central, third lensed image (S. Muller et al. 2020).

The system is a compound gravitational lens, with two distinct lensing systems involved (J. E. J. Lovell et al. 1996). The most prominent one is a foreground face-on spiral galaxy z=0.89 that is also responsible for molecular absorption features (T. Wiklind & F. Combes 1996). The detection of additional HI and OH absorption revealed a second intervening galaxy at z=0.19 (J. E. J. Lovell et al. 1996), which should have a limited influence on the lensing effects. Specifically, studies suggest that its contribution to the gravitational lensing phenomenon is relatively minor, mainly due to its lower mass and distance compared to the main lensing galaxy at z=0.89. Consequently, its impact on the overall lensing dynamics and image distortion of PKS 1830–211 is considered negligible (e.g., J. N. Winn et al. 2002).

Despite the rich set of observations collected for PKS 1830–211 at several wavelengths (radio, optical, X-rays and γ -rays), the measurement of the temporal delay between the A/B components (hereafter τ_{AB}) remains uncertain, with several estimates debated in the literature (T. D. van Ommen et al. 1995; J. E. J. Lovell et al. 1998; T. Wiklind & F. Combes 2001; A. Barnacka et al. 2011; A. Neronov et al. 2015; A. Barnacka et al. 2015; J. Abhir et al. 2021; S. Muller et al. 2023; S. Agarwal et al. 2025; S. M. Wagner et al. 2025). In our previous study (A. A. Abdo et al. 2015, hereafter Paper I), we reported no convincing evidence for lensing effects in the γ -ray lightcurve between 2008 – 2011. Following a prolonged

 γ -ray high state in 2019–2020 (S. Buson & D. Constantin 2019), we initiated a multiwavelength campaign including X-ray and radio observations (S. Buson et al. 2019). The results of our follow-up monitoring at 43 GHz with the Very Long Baseline Array (VLBA) follow-up are presented in Spingola et al. (in prep., PAPER III). In this paper (PAPER II), using over a decade-long legacy Fermi-LAT observations and advanced time-series techniques, we resolve the long-debated γ -ray lensing properties of this system, and unambiguously measure the macrolensing time delay τ_{AB} along with limits in the magnification ratio (early findings appeared in M. De Toma 2023; M. De Toma et al. 2025).

The paper is organized as follows. Sec. 2 offers an overview of the current state of the art. In Sec. 3 describes the *Fermi-LAT* observations and data analysis. Sec. 4 introduces time-series methods for estimating the time delay and presents a novel approach to compute the macrolensing magnification ratio. Sec. 5 outlines the strategy for assessing the local and global statistical significance of the findings. In Sec. 6 we present the results. Our new findings are discussed in the context of previous discrepancies in delay estimates in Sec. 7, and of claimed microlensing effects and variability of the magnification ratio in Sec. 8. Sec. 9 concludes summarizing the main results.

2. TIME DELAY AND MAGNIFICATION RATIO

Gravitational lensing is an achromatic phenomenon, implying that the same lensing delay should be measured consistently across different wavelengths. This assumption holds provided that the overall electromagnetic emission of the blazar originates from a common emission region and that any effects due to smaller lens structures, such as microlensing, are negligible. The lively literature debate about τ_{AB} in the PKS 1830–211 system highlights the complexity of this system. Several methodologies have been employed to infer the time delay associated with the macrolensing effect.

• Delay estimates based on radio observations. The advantage is that instruments with sufficient resolution allow us to spatially separate the A and B components and directly measure the flux of the individual images. Time-series analysis, dispersion-like methods, χ^2 minimization or regression techniques applied directly to the resolved light curves. However, observations in the radio band are challenging to schedule. Generally they encompass a limited time span (< 1 year), with few visits of irregular cadence.

- Delay measurements based on γ-ray time series analysis. Although currently operating γ-ray instruments lack the arcsecond-imaging resolution to spatially resolve the individual lensed components, the strongly variable emission from the blazar, combined with regular long-term flux monitoring, can reveal lensing effects. Light rays originating from the different lensed images follow slightly different paths and thus arrive at the observer with a time delay relative to each other. These delays introduce distinctive time patterns in the lightcurves (LCs), which can be used to study gravitational lensing and related physical properties.
- Predictions inferred from the modeling of the lens system; however, no consistent lens model has been established so far for this system. The culprits are mostly the large uncertainties in the time delay, τ_{AB} , and the lens position. One of the major challenges comes from the location of PKS 1830–211, which lies near the Galactic plane. The vicinity to the galactic center (l= 12.2°, b= -5.7°), makes optical identification difficult as optical observations are affected by dust extinction and by contamination by the Milky Way.

Figure 1 summarizes the claimed estimates of τ_{AB} based on radio observations (black), γ -ray time series (gray), and lens modeling (yellow). We anticipate that, for completeness, the upper row reports the value derived from this study (green; 6.3). Radio-based values converge toward an average¹⁶ $\tau_{AB} = 25.0 \pm 2.3$ days. Estimates at γ -rays were controversial, with multiple τ_{AB} values proposed, not always consistent with each other. In some cases, no significant evidence for a trailing component was found (PAPER I, J. Abhir et al. 2021).

The magnification ratio, defined here as the ratio of the fluxes of the leading and trailing components $\mu = F_A(t)/F_B(t+\tau_{AB})$, ranges between 1.0–2.0 according to radio-based estimates (T. D. van Ommen et al. 1995; B. Frye et al. 1997; J. E. J. Lovell et al. 1998; T. Wiklind & F. Combes 1998; S. Muller et al. 2020, 2023). Previous measurements carried out at γ -rays appeared in tensions with this value, with μ_{γ} ranging between $\sim 2-7$ and invoked also microlensing effects (A. Neronov et al. 2015; A. Barnacka et al. 2015; S. Agarwal et al. 2025).

3. FERMI-LAT OBSERVATIONS AND ANALYSIS

The Fermi-LAT data are reduced with the Python package fermipy (v1.2.0, M. Wood et al. 2017), using the P8R3_SOURCE_V3 instrument response functions (IRFs W. B. Atwood et al. 2009; P. Bruel et al. 2018). We select photons of the Pass 8 SOURCE class, in a region of interest (ROI) of $10^{\circ} \times 10^{\circ}$ square, centered at the target. Events are selected within the time span 2008 August 04 to 2023 August 22 (MJD 54682-60178). To minimize the contamination from γ rays produced in the Earth's upper atmosphere, a zenith angle cut of $\theta < 90^{\circ}$ is applied, along with standard data quality cuts (DATA_QUAL > 0)&&(LAT_CONFIG == 1). Due to the vicinity of the target to the galactic center, a lower energy cut of ≥ 0.2 GeV is applied to mitigate the impact of the bright emission from the galactic components. The ROI model includes all Fermi-LAT Fourth Source Catalog Data Release 3 sources (4FGL-DR3, S. Abdollahi et al. 2022) located within 15° from the ROI center, as well as the Galactic and isotropic diffuse emission 17 (gll_iem_v07.fits and iso_P8R3_SOURCE_V2_v1.txt).

The best-fit ROI model is obtained by performing a binned maximum likelihood analysis in the 0.2-300 GeV energy range, over the entire time range considered here. We use the "gta.optimize" method in fermipy multiple times, which enables to fit the data, while progressively freeing model parameters. In the analysis, the test-statistics (TS) is defined as $2\log(L/L_0)$, where L is the likelihood of the model with a point source at a given position and L_0 is the likelihood without the source (J. R. Mattox et al. 1996).

The Fermi-LAT LC used in the time-series analysis is produced with a 1-day binning. In addition, we built a 28-day bin and adaptive binning LC for illustrative purposes (Section 7.1.3). For the likelihood fits of the time bins, the best-fit ROI model obtained from the entire time-interval analysis is adopted. We first attempt a fit allowing variation in the normalization of the target and of all sources in the inner 3° of the ROI, along with the diffuse components. If the fit does not converge, the number of free parameters is progressively restricted in the fit in an iterative way until the fit successfully converges. We consider the target source to be detected when TS>1 in the corresponding time bin (see e.g. P. Peñil et al. 2025b). Whenever this condition is not fulfilled, a 95% confidence upper limit is reported. These are denoted by down arrows in the plots of the LCs.

¹⁶ The estimate from T. D. van Ommen et al. (1995) was excluded, as likely affected by contamination from the Einstein ring. Similarly, we excluded the result from A. Neronov et al. (2015), adopting instead the original analysis by J. E. J. Lovell et al. (1998) based on the same data.

¹⁷ LAT Background Models

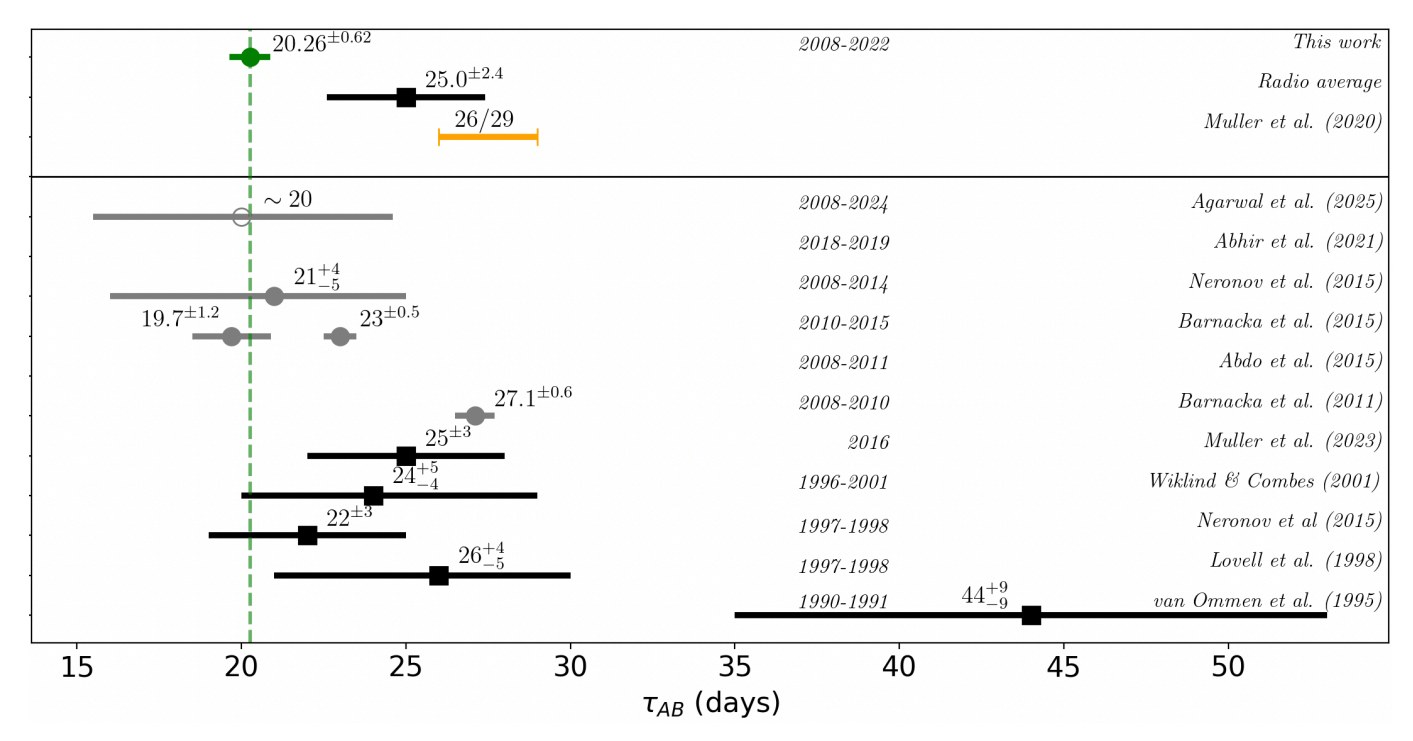


Figure 1. Estimates of the time delay τ_{AB} between the A and B images of PKS 1830–211. The value measured in this work (green) is in mild tension with the radio-average estimate from the literature (black), and with predictions from lens modeling based on radio observations (yellow). The lower panel reports γ -ray estimates (gray, filled circles), and radio estimates (black, filled squares). The study of S. Agarwal et al. (2025) reports an approximate delay estimate, while in our previous work, PAPER I, and of J. Abhir et al. (2021), no delay measurement was inferred. The corresponding observational time windows and references are reported in italics.

Given the vicinity of the target to the ecliptic, and the Galactic plane, we apply a further filtering of the LCs data in order to optimize the number of flux points with better signal-to-noise ratio information. To mitigate possible contamination by the quiet Sun emission, we discard time intervals during which the Sun passes closer than 8° from the ROI center (A. A. Abdo et al. 2011). In the LCs used in the time-series analysis, we retain only points with relative error less than 100% and with TS> 1.

4. TIME-SERIES ANALYSIS

4.1. The auto-correlation function

The auto correlation function (ACF) is a widely used method to quantify the similarity or correlation between a time series and a time shifted copy of itself, i.e. the ACF is a function of this time shift or "lag". We adopt the "local" discrete ACF (DACF_L), an alternative definition of the ACF, which has been shown to be more effective compared to the standard DACF definition in measuring time lags in AGN LCs (W. F. Welsh 1999). The DACF_L includes only those values of the time series a_i that overlap at a given lag, $\tau_m = m\Delta t$, to determine

the mean and standard deviations. It is defined as:

DACF_L(
$$\tau_m$$
) = $\frac{\frac{1}{N-m} \sum_{i=1}^{N-m} (a_i - \bar{a}_1)(a_{i+m} - \bar{a}_2)}{d_1 d_2}$ (1)

where

$$d_1 = \left[\frac{1}{N-m} \sum_{i=1}^{N-m} (a_i - \bar{a}_1)^2 \right]^{1/2}$$
 (2)

$$d_2 = \left[\frac{1}{N-m} \sum_{i=m+1}^{N} (a_i - \bar{a}_2)^2 \right]^{1/2}$$
 (3)

$$\bar{a}_1 = \frac{1}{N-m} \sum_{i=1}^{N-m} a_i, \qquad \bar{a}_2 = \frac{1}{N-m} \sum_{i=m+1}^{N} a_i,$$
 (4)

where the time series a_i is sampled at discrete times t_i (i = 1, ..., N) with equal sampling $(\Delta t = t_{i+1} - t_i)$.

4.2. Macro trends and detrending method

Often blazars' LCs are characterized by a dominant low-frequency power due to a red-noise component, along with the high-frequency fluctuations. The DACF tends to exhibit a smooth and long-tailed decay, reflecting the stochastic nature and long-timescale variability of the blazar's emission. Overall, the presence of strong red-noise variability can smooth or wash out any sharp

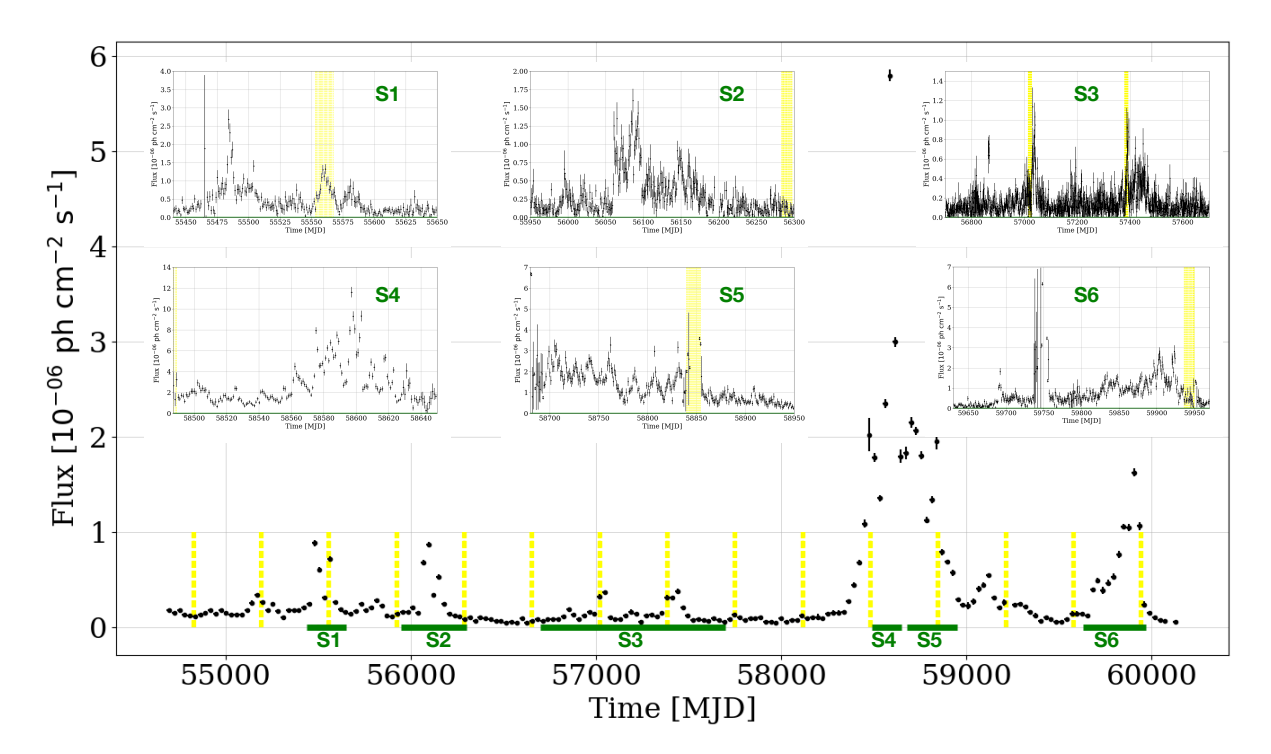


Figure 2. Strong variability is evident throughout the entire 28-day bin LAT LC of PKS 1830-211 shown in the main panel. The six active states utilized in the time-series analysis (green) are listed in Table 1. A close-up view of these segments is presented in the insets, using a 1-day binning. Dashed yellow lines indicate the time intervals when the Sun is within 8° of the ROI center, which were censored in the time-series analysis. Down arrows represent 95% upper limits.

features in the DACF that might arise from periodic or quasi-periodic signals.

A viable strategy to minimize the impact of the macrotrends consists in applying a detrending that "prewhitens" the data. This can be performed by subtracting a polynomial fit or by applying a differencing operator to the data in order to obtain a locally stationary signal as already investigated by W. F. Welsh (1999). We develop a new detrending technique based on a spline function. The latter is an interpolation method that infers and subtracts slow variability using a piecewise polynomial function, cubic in this case. The choice of the spline binning is guided by simulations, which, specifically for the case at hand, showed that a 15-day spline bin provides the best performance (M. De Toma 2023).

4.3. Strategy for choice of time intervals

When investigating periodic or quasi-periodic patterns in an astrophysical object's LC, researchers often analyze one LC data-segment, either the longest at hand or the most variable one. While this approach can seem rigorous, in the presence of strong variability and stochastic processes, the true global significance of any detected pattern is hard to quantify (S. Vaughan et al. 2016). Red-noise dominated LCs can easily pro-

duce few-cycle modulations that appear locally significant, and the probability of detecting such false positives increases when a large ensemble of such sources is available (Appendix A). Unless there are well-motivated priors favoring specific sources or time scales, such approach can lead meaningful findings only when coupled with a rigorous way to account for the look-elsewhere effect (P. Peñil et al. 2020, 2024a; S. Adhikari et al. 2024; P. Peñil et al. 2025; P. Peñil et al. 2025c,d; S. Adhikari et al. 2025; P. Peñil et al. 2025a).

In this study, we adopt a more balanced strategy, applying the time-series analyses to several distinct, non-overlapping LC-data segments which qualitatively display well-defined time-variable structures. Our strategy is not only more robust and conservative but also offers other advantages. On the one hand, we can test possible variations of the time patterns over time; on the other hand, observing the same one consistently across multiple segments corroborates its authenticity.

The choice of the number of data points to use in a time-series analysis depends on several factors. W. F. Welsh (1999) shows that a reasonable LC length should cover at least ~ 10 times the lag of interest. In the case of PKS 1830–211, earlier studies and lens mod-

eling predictions offer an educated guess for the delay timescale τ_{AB} around 20 to 30 days. Consequently, we select segments that span ~ 200 days, and explore lags between 10 to 80 days. Simulations demonstrate that further increasing the length of a LC dominated by red noise may not lead to a significant improvement in the time pattern measurement (W. F. Welsh 1999). The reason is that the DACF is primarily influenced by the segments of the LC with the strongest variability, while the contribution from comparatively less variable parts becomes minimal or negligible. In particular, when the uncertainty of the correlation measure is dominated by stochastic noise, segmenting the data for analysis is advantageous. Following these prescriptions, we select the six most active data segments which are listed in Table 1 and highlighted as the insets in Figure 2.

5. METHODOLOGY FOR STATISTICAL SIGNIFICANCE AND TIME DELAY ESTIMATE

5.1. Local significance of the DACF peaks

To estimate the significance of time lags in a given LC segment, we generate 10⁴ mock LCs using the method by D. Emmanoulopoulos et al. (2013), described in Cristarella Orestano et al. (in prep.)¹⁸. These simulated LCs match the power spectral density (modeled as a power law, PSD $\sim 1/f^{\alpha}$) and probability distribution function (PDF) of the given LC segment. To account for uneven sampling due to data gaps, we apply the real data's time sampling to the mocks. Then, we compute the DACFs of these mock LCs. For each lag τ , we compare the DACF(τ) value found for PKS 1830-211 with the distribution of mock-DACF(τ) values. For every tested τ , the DACF(τ) distribution is fitted with a Gaussian function, to infer the likelihood of observing a value similar to that of PKS 1830-211 by chance. The performance of the methodology were tested on simulated data (see M. De Toma 2023), where we injected a known delayed signal into mock LCs (after detrending) and added flux-dependent white noise with standard deviation equal to the error estimates of the observational data. The method recovered the injected delay with significance $> 5\sigma$ in more than 80% cases, with no spurious delays observed persistently above 2σ . In the following, we define a DACF peak as a lag that shows local significance $> 2\sigma$. Unless otherwise stated, the DACFs have been computed with a time bin of one day.

5.2. Global significance of the DACF peaks

Random fluctuations in stochastic variability can as well produce significant DACF peaks at any lag (Appendix A). These chance probabilities can be estimated by Monte Carlo simulations where the same number of peaks as identified in the real-data DACFs are randomly distributed between lag 10 and 80. Assuming a peak lag uncertainty, or width $\Delta \tau$, there will be $70/\Delta \tau$ possible positions in the DACFs. We require all 6 DACFs to show a peak in the same bin, as a delayed signal arising from macro-lensing effect is expected to produce a peak at the same lag in all segments. Although choices of lag range or peak threshold introduce some arbitrariness, this approach avoids assumptions about the LC variability itself.

5.3. DACF peak properties

The time lag properties of significant DACF peaks are derived by fitting a Gaussian function to the real-data DACF peak, obtaining the time lag estimate, peak height (i.e. amplitude), and width. The same analysis is then applied to the simulated LCs and the standard deviation of the mock-DACF fitted parameters is used to estimate the uncertainties for the corresponding PKS 1830–211 results, taking both statistical and stochastic variability into account.

6. RESULTS

6.1. Long-term LC and DACF

The long-term 1-day binned LC, spanning MJD 54682 to MJD 60178, is shown in Figure 2, with the corresponding DACF displayed in Figure 3. These are included for illustration purposes only and not used in estimating gravitational lensing effects, except for consistency checks. Although in this DACF several peaks exceed a local statistical significance of 5σ , with one at ~ 20 days reaching $> 10\sigma$, their global significance is difficult to assess, as the contribution from stochastic variability is hard to disentangle. This is because the long-term LC includes both quiescent and highly active phases, making it overly simplistic to model the entire period with a single PSD. We address this issue by examining the LCs of two similarly bright blazars in Appendix A. Moreover, the large flux variability across the LC results in the overall DACF being dominated by the brightest epoch, i.e. the flaring episode around MJD 58600 (Section 6.2).

6.2. Segments DACFs results

DACFs of the six selected data segments are shown in Figure 4 along with the statistical significance thresholds obtained as described in Section 5.1. The fact that the

¹⁸ Available at: https://github.com/PaoloCO42/Emmanoulopoulos-Light-Curve-Simulations

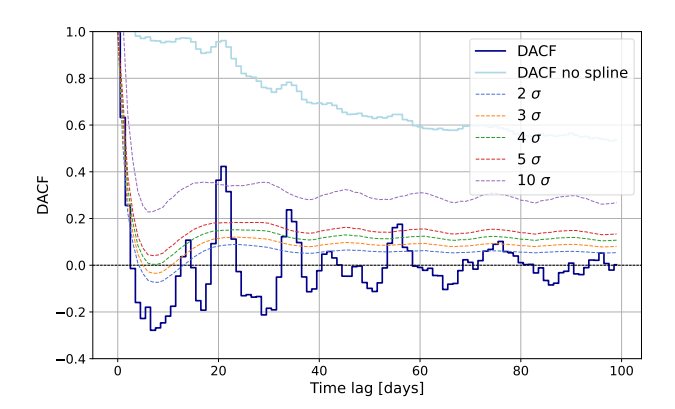


Figure 3. DACF of the long-term 1-day bin LAT LC (MJD 54682-60178) of PKS 1830-211 is shown in cyan. The DACF obtained by the detrended LC is shown in blue, along with the local significance levels.

DACF of segment 4 in Figure 4 is almost identical to the DACF of the long-term LC (see Figure 3) confirms that the latter is dominated by the strong activity in that segment.

Time lags were estimated individually for each of the six data segments as described in Section 5.3. Among those with local significance above 2σ , only one, around 20 days, shows a DACF peak that is consistently present across all segments. The best-fit peak values for this lag are reported in Table 1, for each segment, along with uncertainties estimated from simulations. Following Sec. 5.2, we estimate its global chance probability. The observed number of peaks in the six segment DACFs is 1, 2, 1, 4, 2, and 1, respectively. Assuming a typical peak width of $\Delta \tau \sim 5$, this yields a global chance probability of 2.5×10^{-5} . We interpret the observed time lag of ~ 20 days as arising from macrolensing effect and, thus, as representing τ_{AB} . Radio studies have indicated that the northeast component A (leading) precedes the southwest component B (trailing). However, from the γ ray analysis we cannot unambiguously determine which component leads.

6.3. τ_{AB} time delay

The values estimated for τ_{AB} in Table 1 for the six segments are consistent with each other, within their uncertainties (see Figure 5). Furthermore, one may note that even if the DACF lag estimate for the brightest segment 4 has overall lower statistical errors due to reduced measurement noise than for other segments, the stochastic uncertainty is about the same. This shows that not accounting for stochastic effects would result in an underestimation of the uncertainties.

The impact of stochastic variations can be mitigated by combining the DACFs of the different data segments. This was done by normalizing each data segment to the same mean and then calculating a DACF for the combined LC. In this way, most of the erratic correlations get averaged out. The combined DACF is shown in Figure 6, while the DACFs of individual segments are shown in Figure 7. The peak around 20 days is less affected by this averaging process, strengthening its identification as a genuine, repetitive time pattern, attributable to the presence of a trailing component produced by the gravitational lens. The time lag for the combined LC was estimated with the same method as for the individual segments. The Gaussian fit to the correlation peak yielded a time lag of $\tau_{AB} = 20.26 \pm 0.62$ days and it is shown as an inset in Figure 6. The DACF for the peak is plotted with two time resolutions, a 1-day bin (red) which is the same as the data and a 0.2-day bin (black) which is obtained by oversampling the LC segments by a factor of 10 through linear interpolation. To minimize binning effects, we use fits made to the oversampled LC, while noting that fits to the original data gave consistent results. The error estimate is again based on simulated LCs, containing stochastic red noise with a time-lag component and added Gaussian white noise to mimic measurement errors.

6.4. Triplet effect: stochastic variability

We report the detection of characteristic structure in the DACFs, arising from the coupling of a time-lag component with rapid stochastic variability. In the presence of a time-lag component in the LC, a DACF peak is produced at the corresponding time lag; chance correlations of rapid stochastic variability will also appear as DACF peaks at random time lags. Without any trailing component, two similar LC features, e.g. flares, will result in a single DACF peak at a time lag corresponding to the separation between the two flares. However, if both flares also have a trailing component, there will be not just one DACF peak, but three. A main central peak at the lag where both pairs of peaks overlap and two side peaks at lags where the leading and trailing components overlap. The principle of this "triplet" effect is illustrated in an idealized case in Figure 12 (top). The separation between the triplet components will be equal to the time lag of the trailing component, and their relative amplitude will depend on the lens magnification. If the magnification is e.g. $\mu = 2$ (trailing component with half the amplitude of the leading one), the two side peaks in the DACF will be half the height of the central peak (Figure 12, middle). For increasing magnification ratio, the relative height of the DACF side peaks will

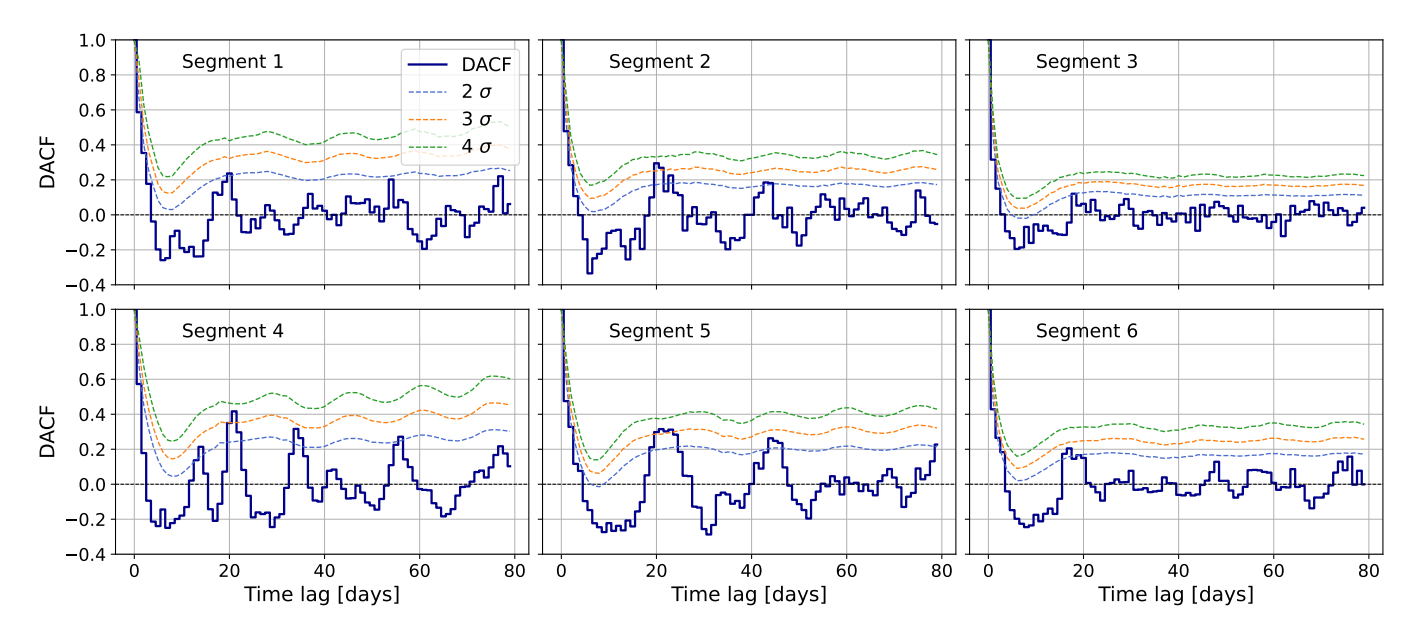


Figure 4. DACF for the six time segments analyzed in this work, listed in Table 1. The respective LCs are shown in the panels of Figure 2. The blue, orange, green dashed lines represent the 2σ , 3σ , 4σ local significance (Section 5.1).

	Start [MJD]	Stop [MJD]	Points	PSD index	Time lag [days]	Sign. $[\sigma]$
1	55440	55650	170	-1.24 ± 0.09	19.58 ± 1.12	≥ 2
2	55950	56300	265	-0.93 ± 0.09	21.49 ± 1.06	≥ 3
3	56700	57700	655	-0.84 ± 0.05	20.22 ± 1.23	≥ 2
4	58487	58650	159	-1.22 ± 0.13	20.96 ± 0.75	≥ 3
5	58680	58950	246	-1.16 ± 0.09	22.03 ± 0.83	≥ 3
6	59630	59970	271	-0.86 ± 0.08	18.72 ± 0.86	≥ 2
1	1–6 combined 1766			$\textbf{20.26} \pm \textbf{0.62}$		

Table 1. Time lag estimates for the six LC segments analysed in Section 4, along with their local significances. Time lag errors are based on simulations reflecting the statistical and sampling properties of the data, adopting the PSD index of the specific LC segment for the simulations (see Section 5)

. The row labeled "1-6 combined" presents the DACF result for a combined LC that includes all segments, each normalized to the same mean flux, shown in Figure 6.

become lower. In simulations with exponential flares, the height of the side components relative to that of the central peak gradually decreased to about 0.3 at magnification ratio 2.5 and then decreased more rapidly with increasing magnification ratio.

In reality, stochastic variability is more complex and leads to a mix of overlapping features. However, investigating the DACFs of PKS 1830–211, one can pinpoint cases that appear to be produced by this triplet effect. Looking at the DACF of data segment 4 (Figure 12, bottom), three peaks at time lags 13.6, 34.5 and 56.1 days have lag separations (20.9 and 21.6 days) that are con-

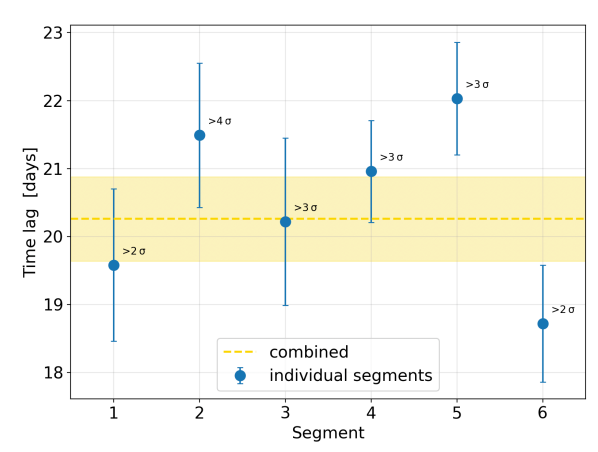


Figure 5. Delay estimates for segments listed in Table 1.

sistent with this effect, although the LC is more complex than the idealized case described above. Since the long-term LC is dominated by the brightest flare (i.e. segment 4), the corresponding DACF also shows features similar to the DACF of segment 4, including features due to the triplet effect.

A more systematic analysis of triplets in the DACF can be done by looking at the distribution of DACF peaks at long time lags. These are dominated by correlations between the different active epochs in the long-term LC. To limit the influence of other parts of the LC, we cross-correlated the six segments with each other and

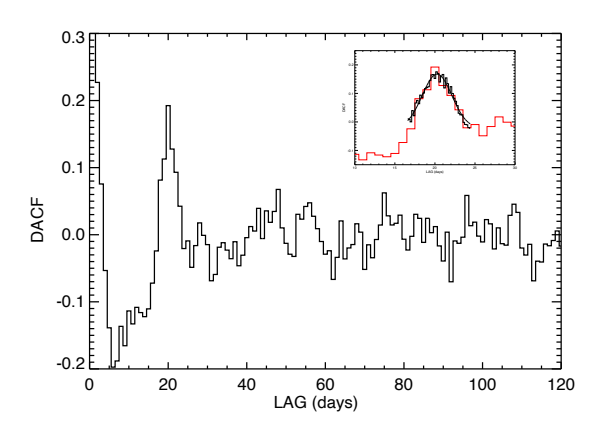


Figure 6. The main panel shows the 1-day binned DACF calculated from a LC that combines all the six data segments. The segments were individually normalized to the same mean flux and detrended by the spline method (Sec. 6.3). The inset at the upper right shows a zoom of the 1-day binned DACF at around ~ 20 days (red) overlaid with the Gaussian fit (black) and the 0.2-day binned DACF (black histogram).

identified correlation peaks consistent with triplet separations. Distinct peaks were qualitatively selected and their positions and widths were estimated by Gaussian fit. An automated procedure was then used to search for triplets among the distribution of peak positions. The extracted distribution, corrected for the lag-dependent bias due to the limited segment lengths, is shown both for simulations and for PKS 1830-211 in Figure 13. The top panel shows the triplet distribution for simulations with (blue) and without (pink) a 20-day time delayed component with magnification $\mu = 1$. The corresponding distribution for PKS 1830-211 in the middle panel gives a qualitative confirmation of the presence of 20day triplets also in the blazar DACF. Since the peak identification procedure is not fully objective, we calculated the DACFs of all the segment mixed correlations and show the average of these in the bottom panel. The peak at about 20 days is a more objective confirmation that the correlation functions contain an overabundance of features separated by ~ 20 days.

6.5. Macrolensing magnification ratio

We introduce a novel method to quantify μ_{γ} , exploiting the whole long-term LC information. Our approach of fitting Gaussian profiles to DACF peaks yields amplitude and width values (Section 5.3), which can be used to estimate the magnification ratio μ_{γ} by comparison with simulations. To model the observed DACF peak amplitude, we generated 100 simulated LCs with 0.1-day resolution, each including a delayed component shifted by 20.0, 20.1, or 20.6 days. These were then re-binned

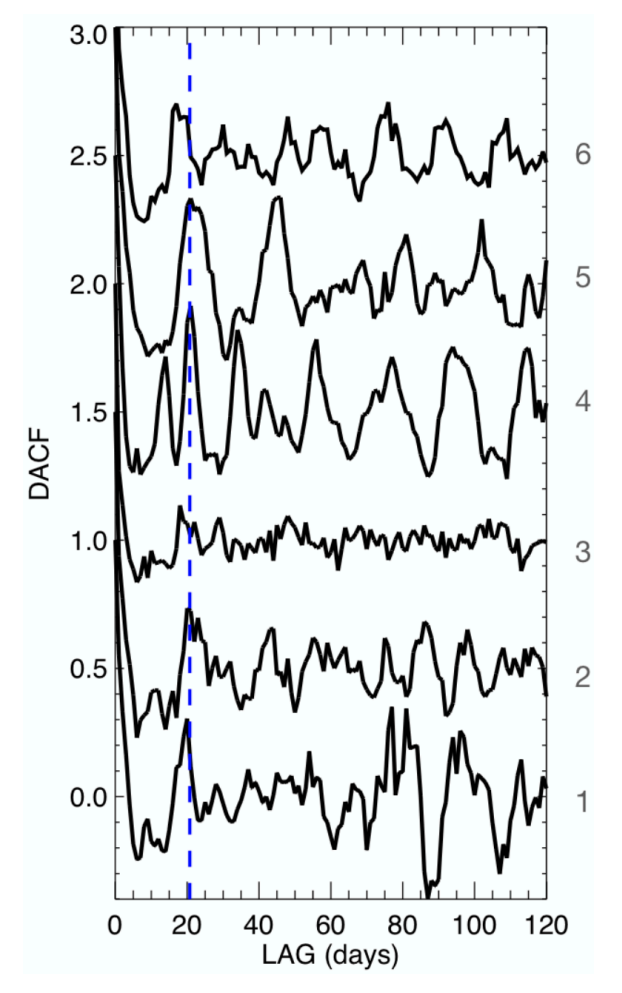


Figure 7. DACFs for the six data segments with the most prominent variability. The curves have been shifted vertically for clarity. The only persistent feature present in all 6 DACFs is indicated by the vertical blue, dashed line at about 20 days.

and resampled to match the 6 observed segments. Since measurement noise strongly affects the DACF peak amplitude, particular care was taken in modeling the measurement errors as a function of flux for the actual observations. Using this error model, flux-dependent Gaussian white and red noise was added to each simulated LC point. This simulation procedure was repeated for 17 magnification ratios between the trailing and leading components, ranging from 5.00 to 1.00.

Figure 8 shows the comparison between the peak height for PKS 1830–211 with the corresponding simulated data. The upper plot shows the results for the combined flux-normalized LC segments shown in Figure 6. The error bars represent the standard deviation for the DACF peaks of the 100 simulations. The wide distribution is dominated by stochastic variations between the different LC simulations. So even if the peak height

and magnification ratio can be determined with a higher accuracy in a particular realization, observational data set, the uncertainty in the estimate of the intrinsic magnification ratio is substantially larger. Taken at face value, the result in Figure 8 would suggest a magnification ratio of $\mu_{\gamma} \sim 1$ with the measured value at 1σ higher than the simulated model. However, the height of a DACF correlation peak is also sensitively dependent on the variance of other variability components in the LC. In our case, this means the measurement noise. If the variance of this component is overestimated, the simulated DACF peaks will be too low. We find that a 20% overestimate is enough to give a shift corresponding to the difference between the simulations and blazar levels in the figure.

Since the relative measurement errors are much smaller in segment 4 than in the other segments, we have repeated the comparison using only the data and simulations for this segment. This is shown in the lower plot of Figure 8. Lower measurement noise yields a higher DACF peak, as visible from the higher overall DACF height values. Although some systematic uncertainty also remains for this case, these findings imply a low $\mu_{\gamma} \lesssim 1.8$, while comparatively larger values of μ_{γ} , as those previously reported, appear unlikely. As discussed in Section 8, the latter may be reconciled with limitations in previous analysis.

An additional result from the DACF modeling of the combined 6 segments is that there is no significant difference in the width (not shown) of the DACF peak between PKS 1830–211 and the simulations. This means that the variations in lag properties reported in Table 1 and visible in Figure 7 are consistent with stochastic and error variability combined with data sampling.

7. COMPARISON WITH PREVIOUS RESULTS

7.1. Reconciling discrepancies in the existing literature

Previous analysis of the Fermi-LAT data yielded inconsistent estimates of the time delay τ_{AB} , with values ranging between ~ 19 and ~ 27 days (A. Barnacka et al. 2011, 2015; A. Neronov et al. 2015; J. Abhir et al. 2021; S. Agarwal et al. 2025), along with claims of microlensing effects. Most of them focused on early mission data up to \sim MJD 57000, that corresponds to data up to our mid-segment 3, and did not account for limitations such as the Sun's γ -ray emission and potential impact of data gaps. These limitations also applied to our initial study, based on the time interval MJD 54700 - 55750, where we found no clear trailing component in the γ -ray LC (Paper I).

We have now re-analyzed the same interval using the method outlined in Section 4 and find a time patter con-

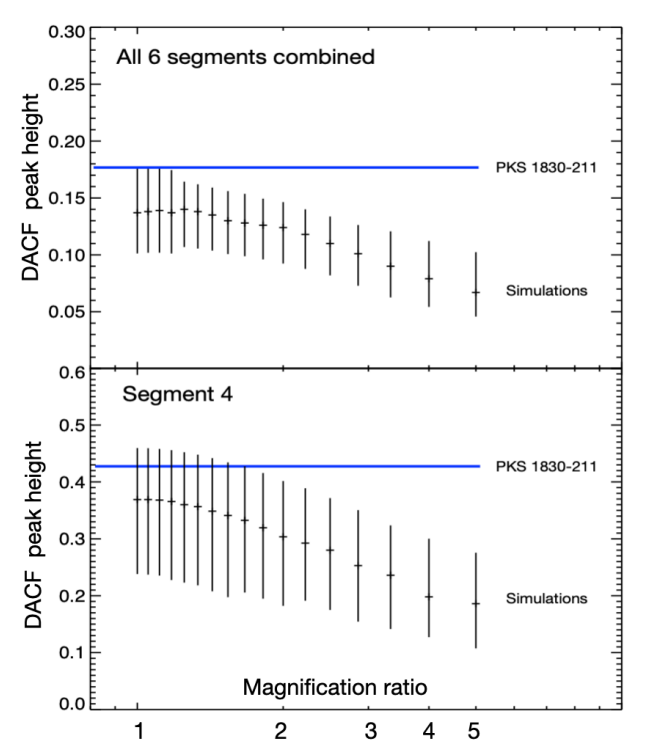


Figure 8. Comparison of DACF peak height for PKS 1830-211 (blue) with corresponding simulations with magnification ratios from 1.00 to 5.00. The median and the asymmetric standard deviation are shown for each simulated magnification ratio (black points). The upper panel shows the result for a LC combining all six data segments, while the lower one is based only on segment 4 where the uncertainties in measurement noise are significantly less than in the other segments.

sistent with $\tau_{AB} \sim 20$ days. As explained in the following, the differing results can be reconciled when considering the improved signal-to-noise time-series data used in this work. We adopt the latest LAT IRFs, Pass8, instead of the older Pass6, apply LC detrending, use a stricter zenith angle cut (90° versus 105°). In addition, we show that times affected by solar contamination within the ROI and data gaps can make it challenging to detect and interpret lensing effects in the blazar.

7.1.1. Confirmation of $\tau_{AB} \sim 20$ days

Figure 10 shows two results: the DACF of the segment analysis (MJD 54700 – 55750), replicating our original study with no censoring of data (light blue), and the analysis after removing the times when the Sun is near the ROI (blue). The peak at about 20 days, with local significance $\gtrsim 3\sigma$, is consistent with the findings presented in this work. In fact, a similar peak at ~20 days was already visible in the DACF computed from a 150-day LC binned at 12 hours, as shown in Figure 3 of PAPER I. In this present work, we deliberated excluded

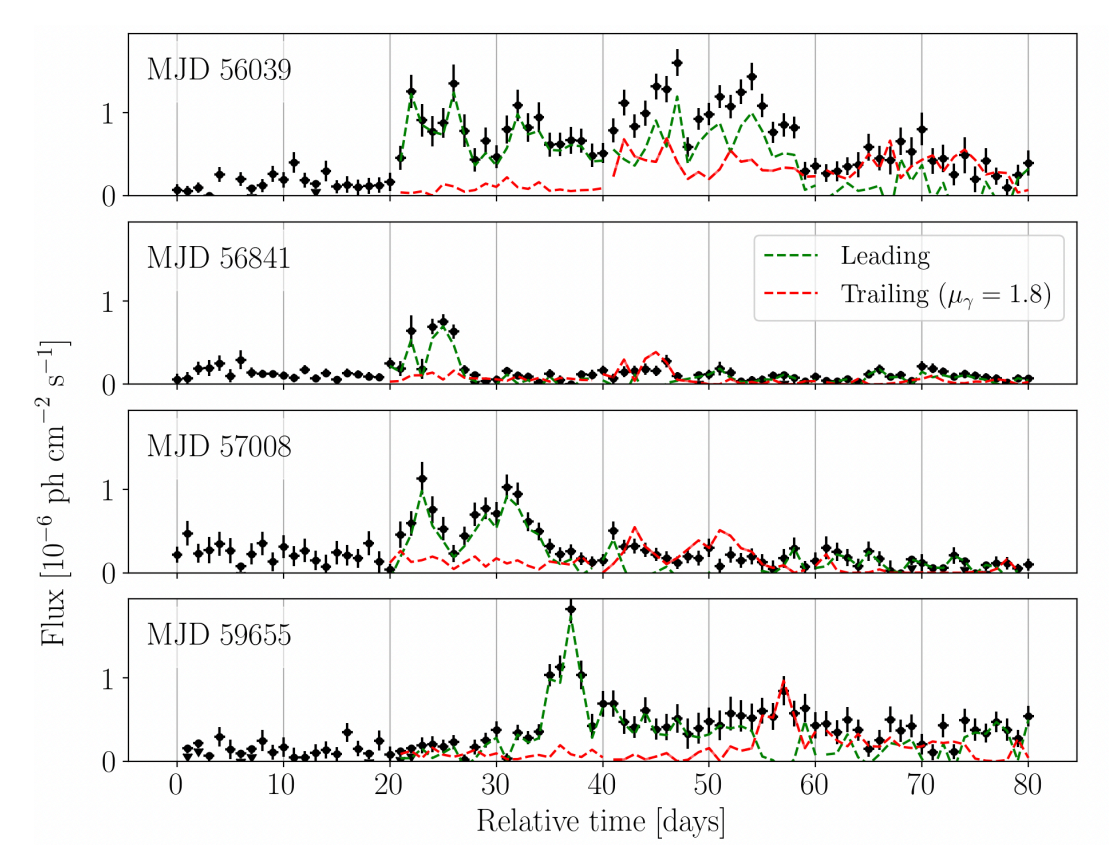


Figure 9. For four relatively sharp, individual flares, the original LC (black points) is decomposed in the leading (green) and trailing (red) components. The latter is obtained by shifting the leading one of τ_{AB} , and assuming a $\mu_{\gamma}=1.8$ (Section 8). Each panel reports in the top left corner the segment's starting MJD.

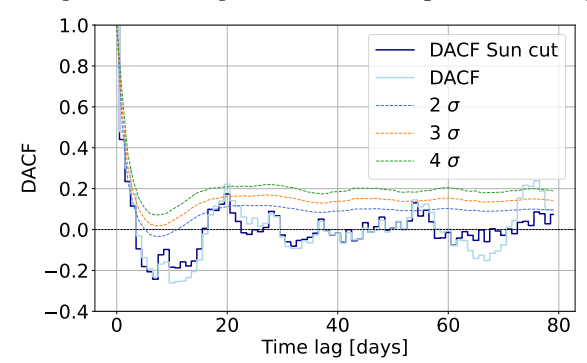


Figure 10. DACF of the LC interval MJD 54700-55750 studied in PAPER I with time intervals during which the Sun is within 8° of the ROI center excluded from the analysis (light blue), and included (blue). See Sec. 5.1.

this data segment initially to avoid potential biases, using it only later as a consistency check.

7.1.2. Contamination by solar activity

An elevated flux state was observed around MJD 55560, previously attributed solely to intrinsic blazar activity. However, our re-analysis reveals substantial solar activity observable during this 20-days period, see Figure 11. If not properly accounted for, so-

lar contamination can distort the blazar flux measurements and bias estimates of the magnification ratio. In this respect, the findings presented here are reliable, as we adopted the conservative approach of excluding data that could be affected by solar emission contamination.

7.1.3. Reduced Fermi-LAT exposure may hamper detection of leading flare component

A relatively bright flare peaking around MJD 55485 (2010-10-16), marked by the horizontal red line in Figure 11, shows no corresponding lensed counterpart. Our re-analysis suggests that this flare may represent the delayed component of a gravitationally lensed flare that eluded detection. That earlier flare could have occurred 20 days earlier, when the LAT exposure (cvan shaded area) toward the blazar region dropped sharply due to a Crab Nebula ToO observation, operated during MJD 55462.67 - 55469.66 (green horizontal line, 2010-09-23 15:49:00 UTC to 2010-09-30 15:49:00 UTC). When the LC points (gray, adaptive binning) are shifted by $-\tau_{AB}$ (-20.26 days), assuming μ_{γ} =1.0, to mimic a potential leading component (red points) of this flare, they are consistent with LAT flux limits. During that time, the only other γ -ray instrument in operation that could

had detected the flare, the AGILE-Gamma-Ray Imaging Detector, was operating in spinning mode, observing only a fraction of the sky (I. Donnarumma et al. 2010).

8. EFFECTS OF MICROLENSING AND μ_{γ} VARIABILITY

Earlier works identified variability in the γ -ray magnification ratio ($\mu_{\gamma} \sim 2-7$) in PKS 1830–211, which was interpreted as microlensing by stars in the lensing galaxy affecting compact emission regions (A. Neronov et al. 2015; A. Barnacka et al. 2015; S. Agarwal et al. 2025). However, this conclusion relied on focusing on a few isolated flare episodes and a simplified flare-based flux ratio method to infer the μ_{γ} between the leading and trailing lensed components. In light of our findings and estimates of $\tau_{AB} \sim 20$ days and $\mu_{\gamma} \lesssim 1.8$, those flaring episodes can be reconciled with macrolensing effect.

The novel method introduced in Section 6.5 provides a more objective approach to quantify μ_{γ} , based on the long-term LC information. Upon qualitatively inspecting four LC segments previously reported to exhibit microlensing or μ_{γ} variability, we do not find convincing indications of such effects. The corresponding 1-day bin LC segments are plotted in black in Figure 9. For each 20-bin interval, we decompose the trailing component (red) assuming a fixed flux ratio¹⁹ of the leading / trailing components, $\mu_{\gamma} = 1.8$. The leading component (green) is computed as the difference between the observed flux and the trailing component. The resulting decomposition traces closely the overall LC trend within statistical measurement uncertainties, and supports lower macrolensing magnification ratios, in agreement with radio-based estimates.

In addition, we note the following. The first flare considered in A. Neronov et al. (2015), at about MJD 55485, was treated in that work as a leading component, but it may be a trailing one, at least in part. Its actual leading component would fall during a period of very low LAT exposure due to a Crab ToO (Section 7.1.3). The second flaring epoch considered, at about MJD 55561, occurred when the Sun was close to the blazar, possibly contaminating blazar's flux measurements (Section 7.1.2, Figure 11). Finally, for the third flare at about MJD 56867, the LC is consistent with a trailing component having a $\tau_{AB} \sim \!\! 20$ days and $\mu_{\gamma} \lesssim 1.8$, as found here (Figure 9).

9. DISCUSSION AND CONCLUSIONS

In this paper, we presented an analysis of \sim 13-yr of Fermi-LAT data, with improved time-series techniques, of the gravitationally lensed system PKS 1830-211. We shed light on the macrolensing properties of this system, reconciling previous controversial findings at γ -rays. The main results are:

- Applying the time-series analysis to six, non-overlapping data segments consistently reveals a recurrent pattern in the data, with best-fit estimate $\tau_{AB} = 20.26 \pm 0.62$. The likelihood of this occurring by chance is as low as 2.5×10^{-5} . This lag in the LC, attributed to gravitational lensing, corresponds to the delay in arrival times between the γ -ray emission from images A and B. Based on simulations, there is no evidence for variations of this lag at γ -ray energies.
- Additional delay patterns emerge from the time series analysis of the LCs, none of which is found statistically significant and, as well, cannot be convincingly attributed to the putative third lensed image of the blazar. The flux of such hypothetical third image, however, would be significantly fainter than the main two (S. Muller et al. 2020).
- In the DACFs of the blazar, we observe a characteristic triplet of peaks. Simulations reveal that this pattern naturally arises by the interplay between rapid stochastic variability and a time-lag component. This corroborates the genuineness of the time-lag observed in PKS 1830-211. It also offers a new approach to identify and study time-patterns in LCs.
- Our novel approach to estimate μ_{γ} exploits the full LC information by using the flux-normalized LC segments and statistical modeling of DACF peak heights to reduce bias and avoid misinterpretation due to isolated flares or incomplete sampling. The estimated $\mu_{\gamma} \lesssim 1.8$, is consistent with radio-based estimates. In addition, we find no supporting evidence for variability in μ_{γ} or microlensing; we discuss that earlier claims may have been biased by analysis limitations.
- The τ_{AB} value inferred at γ -rays is in tension with the average value from radio estimates, as well with predictions from lens modeling, which are based on radio observations too (S. Muller et al. 2020). If the γ -ray/radio delays difference arises from an intrinsic offset between their respective

¹⁹ If a source is split into multiple images, each image (e.g., A and B) is magnified by a different magnification factor relative to the flux of the unlensed source. The ratios of these magnification factors correspond to the flux ratios of the images (P. Schneider et al. 1992).

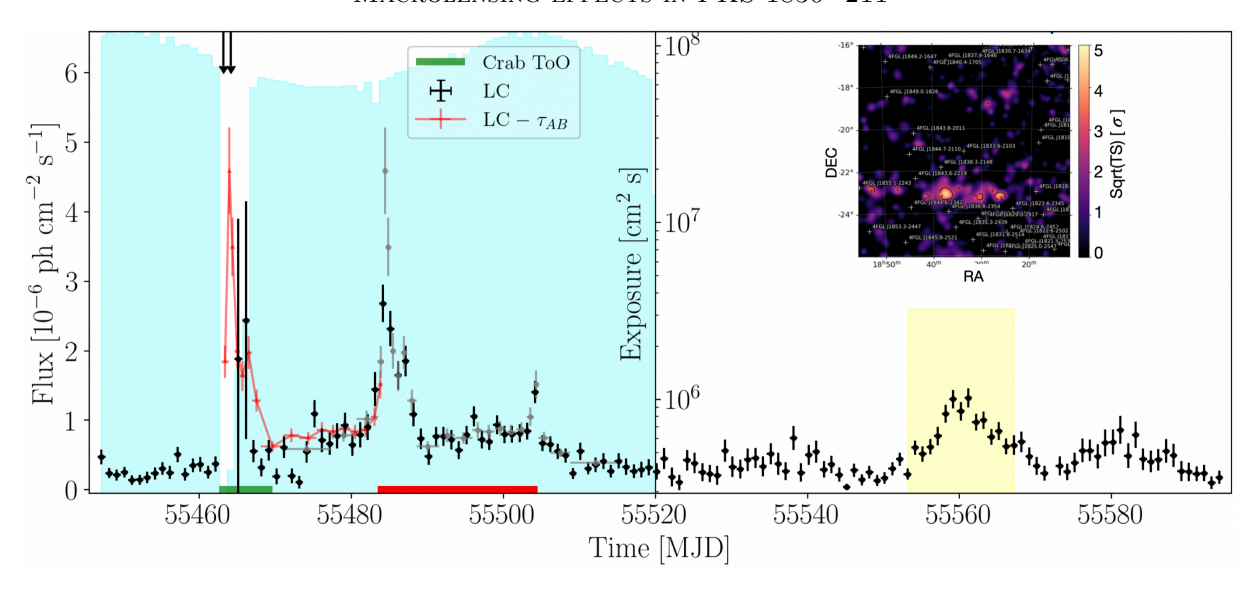


Figure 11. A leading-flare component may have been undetected due to low exposure (cyan) toward the region of PKS 1830–211, during a Crab ToO observation (green, Section 7.1.3). The elevated \sim -20-day flux state observed around MJD 55560, coincides with the passage of the Sun close ($< 2^{\circ}$) from the blazar (yellow area, Sec. 7.1.2). Inset: when inspecting the LAT test-statistics map of the ROI integrating data over the time interval highlighted in yellow, unmodeled solar emission is visible at declination $\sim -22.83^{\circ}$.

emission regions, then, within a singular isothermal sphere lens model, a $\sim 10\%$ difference in the time delay implies a ~ 100 pc offset (projected).

In the case of PKS 1830–211, the γ -ray/radio emission region offset is comparable to that measured for the only other known γ -ray–lensed blazar, B0218+357 (\sim 70 pc; C. C. Cheung et al. 2014). Such separations appear unusually large compared to typical parsec-scale offsets found in other blazars (I. G. Kramarenko et al. 2022). While the observed offsets may reflect underestimated uncertainties in radio-based time-delay measurements, our findings highlight the need for higher-precision radio observations. Although existing radio observations have enabled time-delay measurements of the PKS 1830–211 system, their limited precision has so far prevented to derive comparably accurate time lag measurement, and definitive estimate of the true magnification between the two lensed images.

A time delay difference between radio and γ -rays does not necessarily imply different emission regions. In blazars, it is often observed that γ -rays originate upstream while the accompanying radio emission emerges further away from the black hole. Due to these opacity effects, radio variations often lag behind γ -ray ones, especially in FSRQs, introducing an intrinsic observational offset.

Our study demonstrates that long-term, well-sample LCs, coupled with time-series analysis, enable competitive constraints on gravitational lensing parameters, providing a unique probe into the structure of blazar jet

emission regions on otherwise inaccessible spatial scales. These systems hold potential for time-delay cosmography (S. Birrer et al. 2024). With improved lens models and more precise estimate of the location of the emission region sites, they could provide independent determinations of the Hubble constant, offering complementary insights to those from local distance ladders.

ACKNOWLEDGMENTS

This work was supported by the European Research Council, ERC Starting grant MessMapp, S.B. Principal Investigator, under contract no. 949555, and partially by the German Science Foundation (DFG FOR 5195, grant No. 443220636). CS acknowledges the support by the Italian Ministry of University and Research (grant FIS2023-01611, CUP C53C25000300001) and by the Italian National Institute for Astrophysics (Ob. Fu. 1.05.24.07.04, Ricerca Fondamentale 2024). The Fermi LAT Collaboration acknowledges generous ongoing support from a number of agencies and institutes that have supported both the development and the operation of the LAT as well as scientific data analysis. These include the National Aeronautics and Space Administration and the Department of Energy in the United States, the Commissariat à l'Energie Atomique and the Centre National de la Recherche Scientifique / Institut National de Physique Nucléaire et de Physique des Particules in France, the Agenzia Spaziale Italiana and the Istituto Nazionale di Fisica Nucleare in Italy, the Ministry of Education, Culture, Sports, Science and Technology

(MEXT), High Energy Accelerator Research Organization (KEK) and Japan Aerospace Exploration Agency (JAXA) in Japan, and the K. A. Wallenberg Foundation, the Swedish Research Council and the Swedish National Space Board in Sweden. Additional support for science analysis during the operations phase is gratefully acknowledged from the Istituto Nazionale di Astrofisica in Italy and the Centre National d'Études Spatiales in

France. This work performed in part under DOE Contract DE-AC02-76SF00515.

AUTHOR CONTRIBUTIONS

The three corresponding authors contributed substantially and equally to the analysis, interpretation and preparation of the manuscript.

Facilities: Fermi(LAT)

Software: fermipy (M. Wood et al. 2017), astropy (Astropy Collaboration et al. 2013), TopCat (M. B. Taylor 2005)

APPENDIX

A. BENCHMARKING AGAINST COMPARABLE BRIGHT γ -RAY BLAZARS

The same methodology used for PKS 1830–211 was applied to two other bright variable γ -ray blazars, CTA 102 (4FGL J2232.6+1143) and 3C 454.3 (4FGL J2253.9+1609), using segments matching the duration of those from PKS 1830–211. This allows us to assess potential systematics in the analysis, such as the impact of adopting a fixed PSD spectral index in the simulations. As described in section 4.3, the large range in flux level over the LC also means that the overall DACF is heavily dominated by the brightest epoch, which is the flaring episode around MJD 58600. While using a fixed spectral index, derived from the whole LC segment considered, for the simulations is a reasonable assumption at first order, it does not account for possible variations of the spectral index within time sub-intervals. Applying our methodology on other blazars assesses whether DACF features, similar to those observed in PKS 1830–211, can arise from suboptimal PSD modeling in the mock LCs.

In the case of 3C 454.3, no time lag stands out either from the long-term LC or the individual segments DACFs (left Figure 14). On the other hand, the DACF of the long-term CTA 102 LC displays several time lags exceeding 2σ and up to above 5σ (right Figure 14). Inspecting the LC (not shown), these are likely due to stochastic variability, as they coincide with the separation between major active states. As a reprove, none of these lags appear consistently when analysing segments of active phases as done for PKS 1830–211. As noted in Sec. 5.2, random correlations from stochastic processes can produce peaks at arbitrary time lags, whereas a genuine delayed component would show as a recurrent peak at the same lag across segments. In both objects, no such repeated peaks above 2σ significance are found. This supports the reliability of the adopted methodology and results.

REFERENCES

Abdo, A. A., Ackermann, M., Ajello, M., et al. 2011, ApJ, 734, 116, doi: 10.1088/0004-637X/734/2/116
Abdo, A. A., Ackermann, M., Ajello, M., et al. 2015, ApJ,

799, 143, doi: 10.1088/0004-637X/799/2/143 Abdollahi, S., Acero, F., Baldini, L., et al. 2022, Ap.IS, 260

Abdollahi, S., Acero, F., Baldini, L., et al. 2022, ApJS, 260, 53, doi: 10.3847/1538-4365/ac6751

Abhir, J., Prince, R., Joseph, J., Bose, D., & Gupta, N. 2021, ApJ, 915, 26, doi: 10.3847/1538-4357/abfd33

Adhikari, S., Peñil, P., Domínguez, A., et al. 2025, MNRAS, 540, 1449, doi: 10.1093/mnras/staf783

Adhikari, S., Peñil, P., Westernacher-Schneider, J. R., et al. 2024, ApJ, 965, 124, doi: 10.3847/1538-4357/ad310a

Agarwal, S., Shukla, A., & Sharma, P. 2025, MNRAS, 537, 332, doi: 10.1093/mnras/staf021

Astropy Collaboration, Robitaille, T. P., Tollerud, E. J., et al. 2013, A&A, 558, A33,

doi: 10.1051/0004-6361/201322068

Atwood, W. B., Abdo, A. A., Ackermann, M., et al. 2009, ApJ, 697, 1071, doi: 10.1088/0004-637X/697/2/1071

Barnacka, A., Geller, M. J., Dell'Antonio, I. P., & Benbow, W. 2015, ApJ, 809, 100,

doi: 10.1088/0004-637X/809/1/100

Barnacka, A., Glicenstein, J. F., & Moudden, Y. 2011, A&A, 528, L3, doi: 10.1051/0004-6361/201016175

Birrer, S., Millon, M., Sluse, D., et al. 2024, SSRv, 220, 48, doi: 10.1007/s11214-024-01079-w

Bonvin, V., et al. 2017, Mon. Not. Roy. Astron. Soc., 465, 4914, doi: 10.1093/mnras/stw3006

Figure 12. Illustration of the triplet effect using a simple time series model with sharp identical exponential flares occurring at random times (see Section 6.4).

Top: In the presence of a time lag, two distinct flares (a, c) have corresponding trailing components (b, d) at the lag time. These generate overlapping variability, which increases the stochastic contribution to the LC and the DACF.

Middle: In the DACF, a cross-talk between these flares arises. The red-arrow peak represents the genuine lag, while peaks 1, 2, and 3 emerge from the interplay between noise and this "genuine" lag, forming a triplet structure.

Bottom: This "triplet" effect manifests in the presence of sufficiently pronounced flares, and is clearly visible in segment 4 of PKS 1830–211, where there are three distinct peaks separated by the time lag associated with the trailing component. The actual height of the peaks depends on the magnification ratio, but overlapping variability in a short LC will also modify their amplitudes.

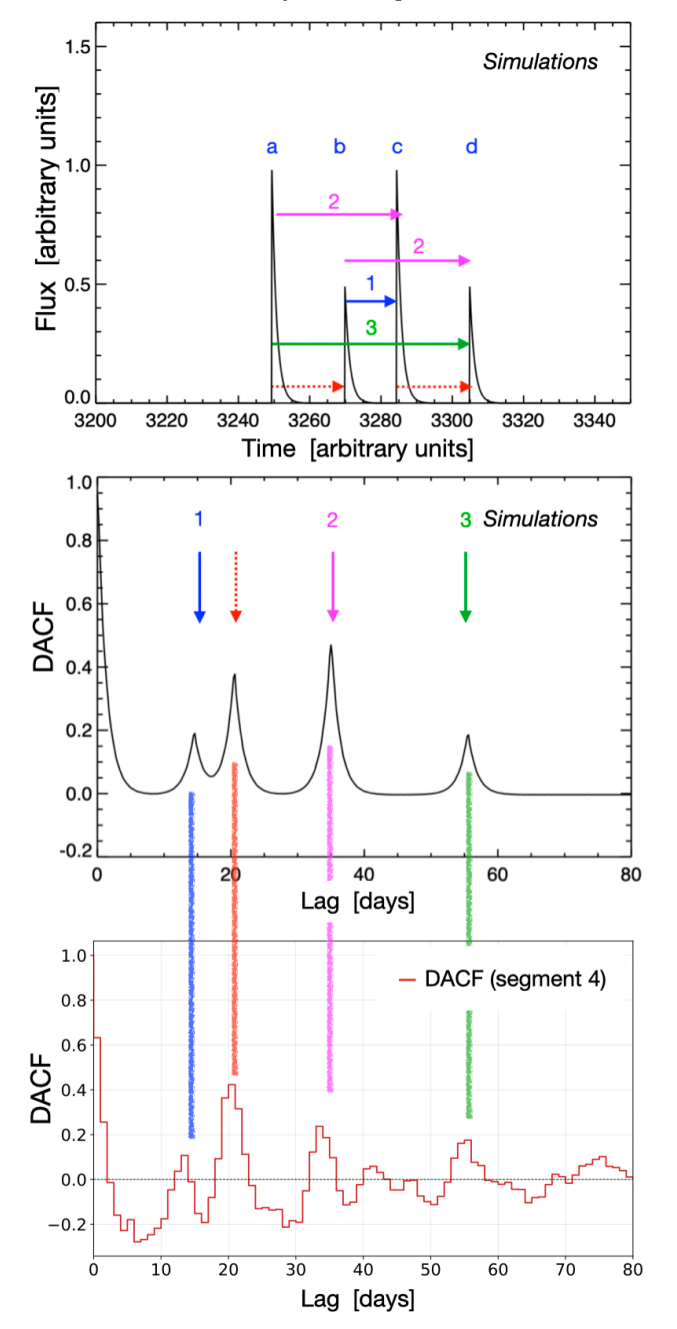
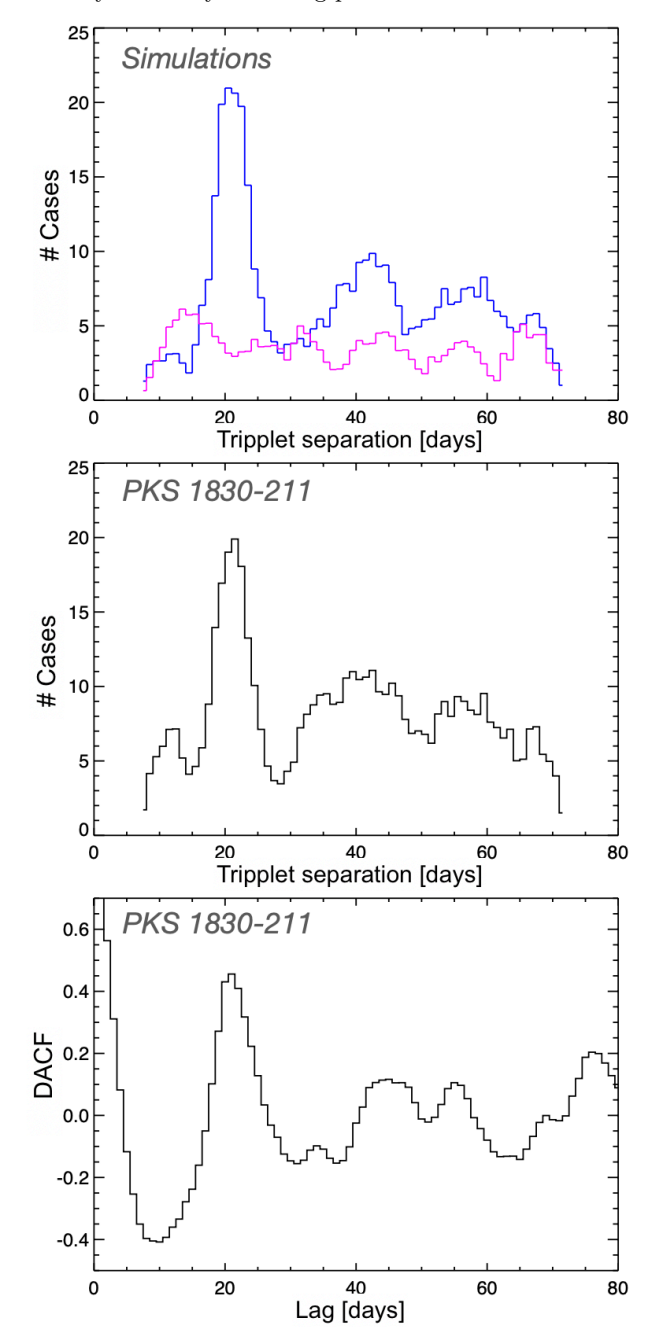


Figure 13. DACF triplets in simulations and in the LC of PKS 1830–211 (see Section 6.4).

Top: Distribution of triplet separations in simulated LCs with (blue) and without (pink) a delayed component.

Middle: Distribution of triplet separations in the mixed correlations between the 6 active epochs in the LC of PKS 1830-211.

Bottom: Average DACF of the mixed segment correlations used to obtain the distribution in the middle plot. The peak around lag 20 is an objective confirmation that the correlations between segments contain an overabundance of features with a separation of about 20 days. The shallower peak around lag 40 can be understood as the higher probability of forming chance correlations between the two outer triplet components (separated by 40 days) and any randomly occurring peaks in the DACF.



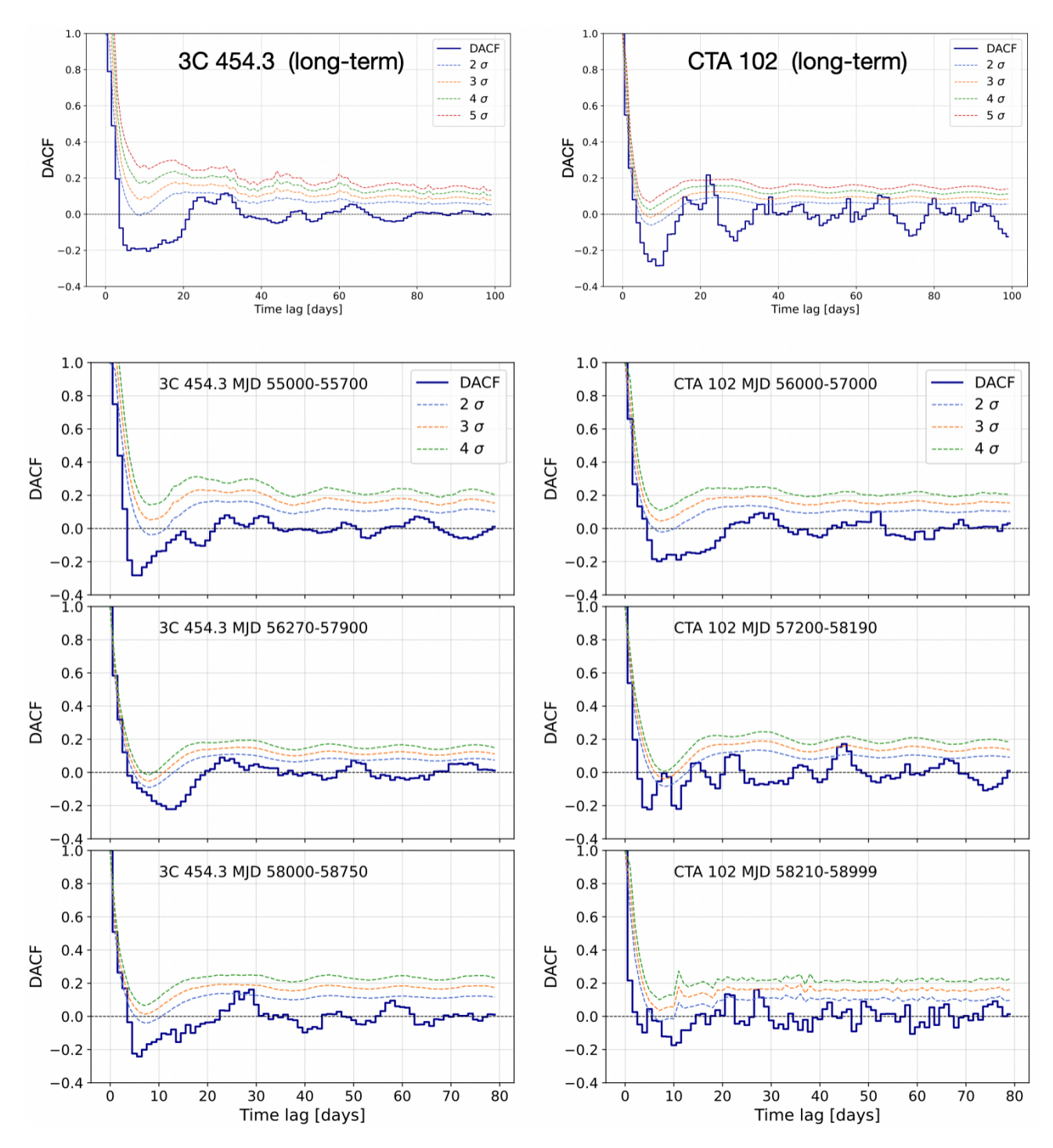


Figure 14. Top: DACFs of the long-term LCs (MJD 54682–60178) for the two brightest LAT γ -ray blazars, 3C 454.3 (left) and CTA 102 (right). Bottom: DACFs and significance curves (Section 5.1) from three LC segments of 3C 454.3 (left; MJD 55000–55700, 56270–57900, 58000–58750) and CTA 102 (right; MJD 56000–57000, 57200–58190, 58210–58999).

- Bruel, P., Burnett, T. H., Digel, S. W., et al. 2018, arXiv e-prints, arXiv:1810.11394. https://arxiv.org/abs/1810.11394
- Buson, S., & Constantin, D. 2019, The Astronomer's Telegram, 13030, 1
- Buson, S., Gokus, A., Wilms, J., et al. 2019, The Astronomer's Telegram, 12696, 1
- Cheung, C. C., Larsson, S., Scargle, J. D., et al. 2014, ApJL, 782, L14, doi: 10.1088/2041-8205/782/2/L14
- Cristarella Orestano et al. in prep.
- De Toma, M. 2023, Master's thesis, University of Pisa
- De Toma, M., Buson, S., Larsson, S., Cheung, C. C., & Orestano, P. 2025, in International Cosmic Ray Conference, Vol. 501, Proceedings of 39th International Cosmic Ray Conference (ICRC2025), 624, doi: 10.22323/1.501.0624
- Donnarumma, I., Vercellone, S., Tavani, M., et al. 2010, The Astronomer's Telegram, 2950, 1
- Emmanoulopoulos, D., McHardy, I. M., & Papadakis, I. E. 2013, MNRAS, 433, 907–927, doi: https://doi.org/10.1093/mnras/stt764
- Frye, B., Welch, W. J., & Broadhurst, T. 1997, The Astrophysical Journal, 478, L25, doi: 10.1086/310538
- Jauncey, D. L., Reynolds, J. E., Tzioumis, A. K., et al. 1991, Nature, 352, 132, doi: 10.1038/352132a0
- Kramarenko, I. G., Pushkarev, A. B., Kovalev, Y. Y., et al. 2022, MNRAS, 510, 469, doi: 10.1093/mnras/stab3358
- Lidman, C., Courbin, F., Meylan, G., et al. 1999, ApJL, 514, L57, doi: 10.1086/311949
- Lovell, J. E. J., Jauncey, D. L., Reynolds, J. E., et al. 1998, ApJL, 508, L51, doi: 10.1086/311723
- Lovell, J. E. J., Reynolds, J. E., Jauncey, D. L., et al. 1996, ApJL, 472, L5, doi: 10.1086/310353
- Mattox, J. R., Bertsch, D. L., Chiang, J., et al. 1996, ApJ, 461, 396, doi: 10.1086/177068
- Muller, S., Jaswanth, S., Horellou, C., & Martí-Vidal, I. 2020, A&A, 641, L2, doi: 10.1051/0004-6361/202038978
- Muller, S., Martí-Vidal, I., Combes, F., et al. 2023, A&A, 674, A101, doi: 10.1051/0004-6361/202245768
- Nair, S., Narasimha, D., & Rao, A. P. 1993, ApJ, 407, 46, doi: 10.1086/172491
- Neronov, A., Vovk, I., & Malyshev, D. 2015, Nature Physics, 11, 664, doi: 10.1038/nphys3376
- Peñil, P., Ajello, M., Buson, S., et al. 2025a, MNRAS, doi: 10.1093/mnras/staf1108
- Peñil, P., Domínguez, A., Buson, S., et al. 2025b, ApJ, 980, 38, doi: 10.3847/1538-4357/ada4b3

- Peñil, P., Torres-Albà, N., Rico, A., et al. 2025c, MNRAS, 539, 993, doi: 10.1093/mnras/staf482
- Peñil, P., Domínguez, A., Buson, S., et al. 2020, ApJ, 896, 134, doi: 10.3847/1538-4357/ab910d
- Peñil, P., Westernacher-Schneider, J. R., Ajello, M., et al. 2024a, MNRAS, 527, 10168, doi: 10.1093/mnras/stad3246
- Peñil, P., Otero-Santos, J., Ajello, M., et al. 2024b, MNRAS, 529, 1365, doi: 10.1093/mnras/stae594
- Peñil, P., Zhang, H., Otero-Santos, J., et al. 2025d, ApJ, 985, 199, doi: 10.3847/1538-4357/adcbab
- Pramesh Rao, A., & Subrahmanyan, R. 1988, MNRAS, 231, 229, doi: 10.1093/mnras/231.2.229
- Refsdal, S. 1964, MNRAS, 128, 307, doi: 10.1093/mnras/128.4.307
- Rico, A., Domínguez, A., Peñil, P., et al. 2025, A&A, 697, A35, doi: 10.1051/0004-6361/202452495
- Schneider, P., Ehlers, J., & Falco, E. E. 1992, Gravitational Lenses, doi: 10.1007/978-3-662-03758-4
- Spingola et al. in prep.
- Subrahmanyan, R., Narasimha, D., Pramesh Rao, A., & Swarup, G. 1990, MNRAS, 246, 263
- Taylor, M. B. 2005, in Astronomical Society of the Pacific Conference Series, Vol. 347, Astronomical Data Analysis Software and Systems XIV, ed. P. Shopbell, M. Britton, & R. Ebert, 29
- van Ommen, T. D., Jones, D. L., Preston, R. A., & Jauncey, D. L. 1995, ApJ, 444, 561, doi: 10.1086/175630
- Vaughan, S., Uttley, P., Markowitz, A. G., et al. 2016, MNRAS, 461, 3145, doi: 10.1093/mnras/stw1412
- Wagner, S. M., Scargle, J. D., Madejski, G., et al. 2025, arXiv e-prints, arXiv:2510.07220, doi: 10.48550/arXiv.2510.07220
- Welsh, W. F. 1999, Publications of the Astronomical Society of the Pacific, 111, 1347, doi: 10.1086/316457
- Wiklind, T., & Combes, F. 1996, Nature, 379, 139, doi: 10.1038/379139a0
- Wiklind, T., & Combes, F. 1998, The Astrophysical Journal, 500, 129, doi: 10.1086/305701
- Wiklind, T., & Combes, F. 2001, in Astronomical Society of the Pacific Conference Series, Vol. 237, Gravitational Lensing: Recent Progress and Future Go, ed. T. G. Brainerd & C. S. Kochanek, 155, doi: 10.48550/arXiv.astro-ph/9909314
- Winn, J. N., Kochanek, C. S., McLeod, B. A., et al. 2002, ApJ, 575, 103, doi: 10.1086/341265
- Wood, M., Caputo, R., Charles, E., et al. 2017, in International Cosmic Ray Conference, Vol. 301, 35th International Cosmic Ray Conference (ICRC2017), 824, doi: 10.22323/1.301.0824